

# Bayesian seismic waveform inversion: Parameter estimation and uncertainty analysis

Wences P. Gouveia<sup>1</sup> and John A. Scales

Department of Geophysics, Center for Wave Phenomena, Colorado School of Mines, Golden

## Abstract

The goal of geophysical inversion is to make quantitative inferences about the Earth from remote observations. Because the observations are finite in number and subject to uncertainty, these inferences are inherently probabilistic. A key step is to define what it means for an Earth model to fit the data. This requires estimation of the uncertainties in the data, both those due to random noise and those due to theoretical errors. But the set of models that fit the data usually contains unrealistic models; i.e., models that violate our a priori prejudices, other data, or theoretical considerations. One strategy for eliminating such unreasonable models is to define an a priori probability density on the space of models, then use Bayes theorem to combine this probability with the data misfit function into a final a posteriori probability density reflecting both data fit and model reasonableness. We show here a case study of the application of the Bayesian strategy to inversion of surface seismic field data. Assuming that all uncertainties can be described by multidimensional Gaussian probability densities, we incorporate into the calculation information about ambient noise, discretization errors, theoretical errors, and a priori information about the set of layered Earth models derived from in situ petrophysical measurements. The result is a probability density on the space of models that takes into account all of this information. Inferences on model parameters can be derived by integration of this function. We begin by estimating the parameters of the Gaussian probability densities assumed to describe the data and model uncertainties. These are combined via Bayes theorem. The a posteriori probability is then optimized via a nonlinear conjugate gradient procedure to find the maximum a posteriori model. Uncertainty analysis is performed by making a Gaussian approximation of the a posteriori distribution about this peak model. We present the results of this analysis in three different forms: the maximum a posteriori model bracketed by one standard deviation error bars, pseudo-random simulations of the a posteriori probability (showing the range of typical subsurface models), and marginals of this probability at selected depths in the subsurface. The models we compute are consistent both with the surface seismic data and the borehole measurements, even though the latter are well below the resolution of the former. We also contrast the Bayesian maximum a posteriori model with the Occam model, which is the smoothest model that fits the surface seismic data alone.

## 1. Introduction

Inverse calculations involve making inferences about models of physical systems from data. As an initial step in solving an inverse problem one must define what it means for a model to fit the data. This requires quantification of the uncertainties in the data, both those due to noise and those due to theoretical (modeling) errors. If a sufficiently fine parameterization of the physical system is used (the model space), there will likely be a large set of models that fit the data, including reasonable and unreasonable models. Here, reasonable means consistent with information that is independent of the data from which the inferences are being made. This a priori information could arise from other observations (e.g., outcrop data indicate a river-dominated fluvial deltaic system, so one may expect continuous sandstone layers), from theoretical considerations (the speed of light is a constant), or from definition (density is nonnegative). Further, this a priori information could be deterministic or probabilistic. The use of probabilistic a priori information, as it is done in Bayesian inference, is a controversial point [Scales and Snieder, 1997]. If the a priori information is deterministic, then one can reasonably look for the smallest confidence sets containing models that fit the data and satisfy this information (as in the work by Stark [1992], for example). On the other hand, Bayesians impose probability densities on the models themselves. These probabilities, which represent measures of degrees of belief, are coupled with the data misfit function (the likelihood function) into a final (a posteriori) probability density on the space of models. A key issue, not addressed in this paper, is when a priori information can reasonably be represented probabilistically. (For additional discussion of this problem, see Scales [1996].) In the Bayesian formulation, questions about uncertainties of subsurface estimates are answered via the a posteriori probability density. If this probability is simple (e.g., Gaussian), this analysis is straightforward. Otherwise, more elaborate procedures such as Monte Carlo sampling may be required.

Here, Bayesian inference is applied to a field seismic data set where we believe that a priori probability densities can reasonably be derived from in situ petrophysical measurements. Further, data and modeling uncertainties are explicitly accounted for. Assessment of the uncertainties associated with the calculation are derived from the a posteriori probability density in three different ways: via error bars on the estimates of the subsurface parameters, pseudo-random realiza-

tions of the subsurface, and marginal probability densities. We also contrast the Bayesian maximum a posteriori model with the smoothest model that fits the data (the Occam model, as defined by Constable *et al.* [1987]), which is obtained via Tikhonov regularization. This illustrates the huge range of models that fits the reflection seismic data alone.

## 2. Reflection Seismic Waveform Inversion

### 2.1. Information and Ambiguity

Consider the P wave impedance, S wave impedance, and density depth profiles in Figure 1. All profiles have been derived from the same field surface seismic waveform data but using two distinctly different techniques. The profiles labeled Bayes were computed via a Bayesian inversion scheme described in section 5 below. This model fits the surface seismic data and a nearby suite of well log measurements, used as a priori information. The profiles labeled Occam were derived from a Tikhonov regularization procedure designed to produce the smoothest model that fits the surface data alone. Figure 1 also shows the elastic response of both models. Notice that the observed data and synthetic seismic traces are alternated in the plot to show the extent to which the models fit the data. The large differences between the models show that many of the features in the Bayesian maximum a posteriori model are not required to fit the surface data. Such features are brought into the solution by the well logs. As we will show in section 6, the Bayesian model estimates and associated uncertainties will be significantly influenced by the well log data, the resolution of which is well beyond that of the surface seismic data. In a sense, we are getting features out of the calculation that we put in via the a priori probability density. (For a detailed comparison of the Bayesian and Occam strategies in the context of waveform inversion, see Gouveia and Scales [1997].)

### 2.2. Formulation of the Problem

Here, we perform a Bayesian inverse calculation to estimate elastic impedance and density profiles from P wave seismic surface data. As has been thoroughly developed by Tarantola [1987], the Bayesian solution of the problem is the a posteriori probability density on the space of models, which we denote by  $\sigma(\mathbf{m})$ . This probability density is the product of two terms. The likelihood function  $L(\mathbf{m})$  defines what it means for a model to fit the data. The second term, the a priori

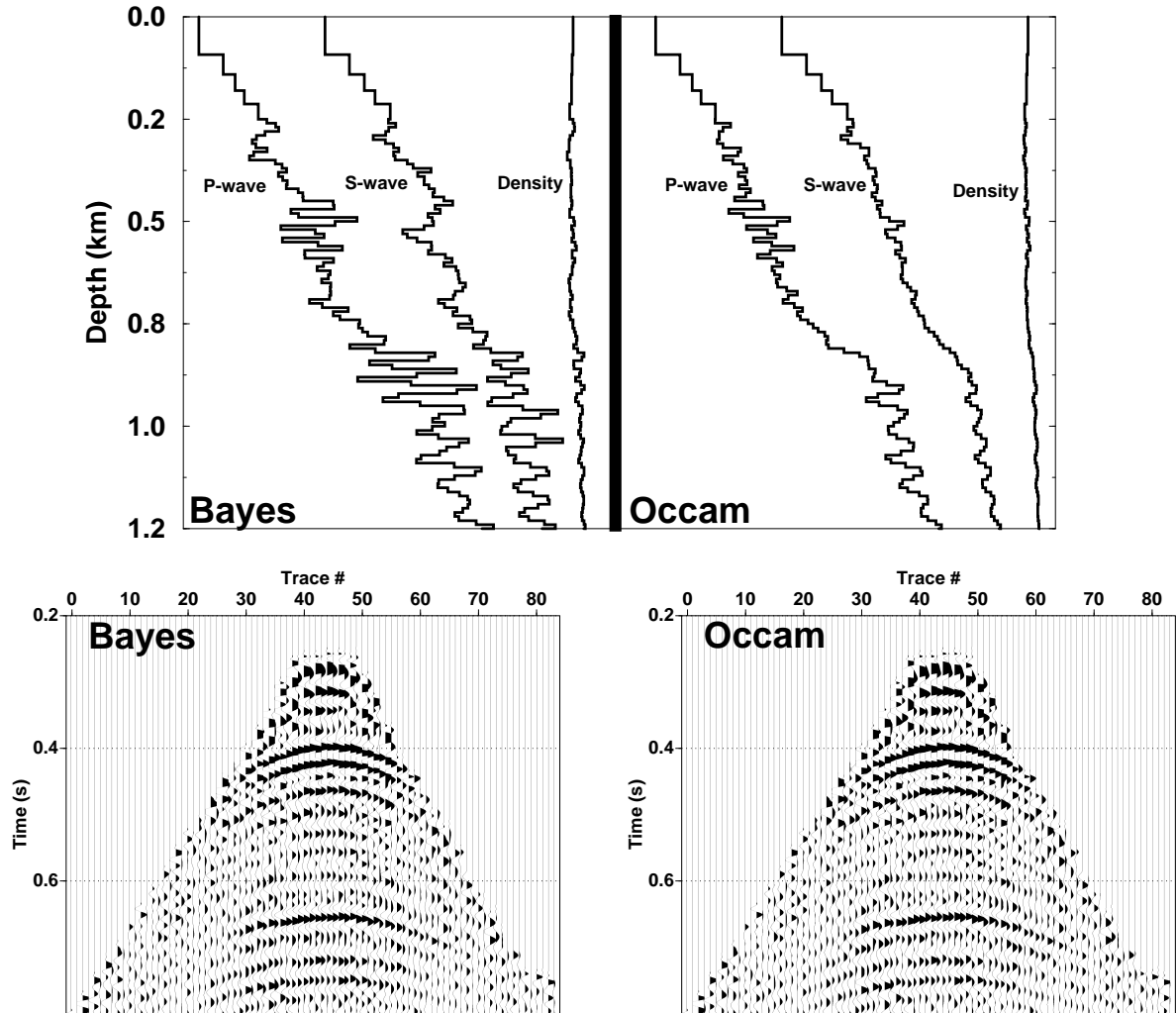


**Figure 1.** (top) Bayes and Occam estimates derived from the same seismic surface data set. Shown are from left to right: P wave impedance, S wave impedance and density profiles. Here, the profiles are simply shown side by side in arbitrary units. (bottom) Field surface seismic data and elastic seismic responses for the Bayes and Occam models. In both gathers, field and synthetic traces are alternated to show the extent to which the model fits the data.

probability  $\rho(\mathbf{m})$ , incorporates information about the subsurface that is independent of the observed data from which the inferences are being made. In the event that the Gaussian model is an acceptable approximation for all uncertainties of the problem, the likelihood function is given by

$$L(\mathbf{m}) \propto \exp \left[ -\frac{1}{2}(\mathbf{g}(\mathbf{m}) - \mathbf{d}_{\text{obs}})^T C_D^{-1} (\mathbf{g}(\mathbf{m}) - \mathbf{d}_{\text{obs}}) \right], \quad (1)$$

while the prior distribution is given by

$$\rho(\mathbf{m}) \propto \exp \left[ -\frac{1}{2}(\mathbf{m} - \mathbf{m}_{\text{prior}})^T C_M^{-1} (\mathbf{m} - \mathbf{m}_{\text{prior}}) \right], \quad (2)$$

where  $\mathbf{g}(\mathbf{m})$  is the seismic forward modeling operator that generates the displacement field given a discretized model  $\mathbf{m}$  of the subsurface,  $\mathbf{d}_{\text{obs}}$  is the observed surface seismic data,  $C_D$  is the data covariance matrix,  $\mathbf{m}_{\text{prior}}$  is the center of the a priori probability density, and  $C_M$  is the model covariance matrix.  $C_D$  and  $C_M$  incorporate the uncertainties in the data (modeling and observational errors) and uncertainties related to the subsurface parameters, respectively. Here, we have adopted such a Gaussian hypothesis, and in section 4 we will describe how we compute these matrices.

For the data we will be treating, it is reasonable to assume that the subsurface can be parameterized in terms of elastic impedances and density in a laterally homogeneous, isotropic model. Thus a suitable choice for  $\mathbf{g}(\mathbf{m})$  is the reflectivity integral modeling operator of *Fuchs and Müller* [1971]. Being an analytic approach, the reflectivity method allows for the calculation of analytic Fréchet derivatives [Gouveia, 1996], which are the derivatives of the forward modeling operator with respect to model parameters. Moreover, the reflectivity method and the procedure to compute its derivatives present a high degree of parallelism, which we have exploited via a network-distributed implementation of the computer codes.

There have been many applications of Bayesian inference in geophysical inverse theory; we mention here only a few to illustrate the spectrum of approaches. For instance, *Mora* [1987] and *Cruse et al.* [1990] compute the maximum a posteriori estimate  $\mathbf{m}_{\text{map}}$  without attempting to estimate the covariance matrices  $C_D$  and  $C_M$ . Thus they offered a single model as the solution of the inverse problem and did not quantify the data or model uncertainties in the calculation.

At another extreme, *Mosegaard and Tarantola* [1995] have shown a very general, albeit synthetic, example of the use of Monte Carlo methods to derive uncertainty estimates by sampling  $\sigma(\mathbf{m})$  without resorting to a Gaussian approximation for this probability. At this time, however, such a procedure is computationally impractical for inversion of reflection multioffset seismic field data.

We steer a middle course between these two extremes. We do assume that all uncertainties can be described by multidimensional Gaussian probabilities, but we go to some lengths to compute these probabilities consistently from the data and prior information. In particular, in the calculation of  $\sigma(\mathbf{m})$  we have taken into consideration data uncertainties, i.e., errors in the data and in the forward modeling procedure. A priori uncertainties in the subsurface parameters are incorporated via a probability density derived from fine-scale well log measurements. However, due to the high computational cost of the seismic forward modeling operator, a global exploration of  $\sigma(\mathbf{m})$  is simply not practical. Therefore we use local, nonlinear optimization techniques to find the model  $\mathbf{m}_{\text{map}}$  and then perform a local analysis of  $\sigma(\mathbf{m})$  in the vicinity of this model. Such an analysis is accomplished by approximating  $\sigma(\mathbf{m})$  with a Gaussian probability density (referred to as  $\sigma_g(\mathbf{m})$ ) about  $\mathbf{m}_{\text{map}}$ , obtained by linearizing the forward modeling procedure about this model. Once this is done, the complete Bayesian picture of resolution is provided by this Gaussian approximation to  $\sigma(\mathbf{m})$

$$\sigma_g(\mathbf{m}) \propto \exp \left[ (\mathbf{m} - \mathbf{m}_{\text{map}})^T C_{M'}^{-1} (\mathbf{m} - \mathbf{m}_{\text{map}}) \right], \quad (3)$$

where  $C_{M'}$  is the a posteriori covariance matrix. Notice that  $\mathbf{m}_{\text{map}}$  is simply the center of  $\sigma_g(\mathbf{m})$  and by itself provides no insight on the resolution of the inverse calculation, which is quantified by  $C_{M'}$ . *Tarantola* [1987] shows that this matrix is given by

$$C_{M'} = [G^T C_D^{-1} G + C_M^{-1}]^{-1}, \quad (4)$$

where  $G$  is the linearization of  $\mathbf{g}(\mathbf{m})$  about  $\mathbf{m}_{\text{map}}$  and  $G^T$  is its transpose.

This paper is structured as follows. In section 3 we introduce the field data used in this calculation. In section 4 we describe the approach taken to quantify the a priori uncertainties associated with the model parameters and the data uncertainties, represented by the model and data covariance matrices. In section 5 we calculate  $\mathbf{m}_{\text{map}}$  and extract error bars and other

measures of uncertainty from the Gaussian approximation to the a posteriori probability density. With this information at hand, interpreters can quantitatively address questions related to the subsurface. The a posteriori probability is the tool for answering these questions.

### 3. Sorrento Data

The surface seismic data and well logs we used were provided by T. Davis of the Colorado School of Mines Reservoir Characterization Project. The seismic data are a small subset of the vertical component data extracted from a nine-component survey acquired at the Sorrento Basin (near the Las Animas Arch, southeast Colorado). Although the inversion software developed as part of this work is able to handle transverse components of the displacement field, the shear data were judged too noisy to be used.

The Sorrento Field reservoir rock consists of Morrowan fluvial sediments, which filled incised valleys during a series of pulses of rising and falling sea level. The geology is stratified down to the reservoir level with subtle structural features. The assumption of lateral homogeneity of the subsurface which we make here is consistent with such a geologic scenario. Section 3.1 describes the regional structural setting and stratigraphy of the Sorrento field.

#### 3.1. Regional Geology

Sorrento Field is located at the eastern flank of the Denver Basin on the northwestern plunge of the Las Animas Arch. Reservoir rocks in this field are fluvial sandstones of Morrowan age that filled incised valleys. According to the geological model developed by *Mark* [1995], these fluvial sandstones represent stacked sequences resulting from a series of sea level rises and falls that alternately deposited sediments and partially removed them by erosion. Mississippian carbonates underly the Morrow interval, and the overlying Pennsylvanian and Permian sections are made up of thick zones of interbedded carbonates, shales, and evaporites.

Both compressional seismic data and regional gravity and magnetic data show that northwesterly and northeasterly faults dominate the structural configuration of Sorrento Field today. Structural features are very subtle, however, and little geological dip is present down to the reservoir level.

#### 3.2. Surface Seismic Data and Well Logs

The source and receiver locations for the Sorrento data acquisition are shown in Figure 2a. The solid dots represent vibrator-source locations, and open dots represent the receiver locations. The circle encompasses the five shot gathers used in the calculation, for which lines 1-8 are active. In this paper we will just show the results obtained with shot gather 1. For a complete description of the results obtained with the Sorrento data, see *Gouveia* [1996].

Among the eight lines recorded for each shot, five were chosen on the basis of their relatively good signal-to-noise ratio. The ones associated with shot gather 1 are shown in Figure 2b. These lines contain the data used in the inversion calculation described in section 4. Field and residual statics corrections along with band-pass filtering were the only processing steps applied to the Sorrento data, which were resampled to a 4-ms sampling interval. The selected shot gathers surround a well denoted MULL 14 (indicated by an arrow in Figure 2a), in which P wave and S wave dipole sonic and density cased hole logs have been acquired. We used these well logs, shown after blocking in Figure 3, to construct the a priori model covariance matrices.

### 4. Quantifying Uncertainties

In the inverse calculation we have considered a depth target zone of 1 km thickness, starting at a depth of 0.25 km. Within this interval the subsurface was parameterized with 100 horizontal layers of 10 m thickness. Each layer is homogeneous and is characterized by P wave and S wave impedances and density. Thus a total of 300 subsurface parameters will be inferred from the Sorrento seismic data and well logs. In this section, we will discuss the error associated with this discretization level, as well as other sources of errors that influence the resolution of the calculation.

We assume that the covariance matrices  $C_D$  and  $C_M$  obtained from fluctuations in the observations (seismic data and well log data) suffice to characterize the uncertainties associated with the inverse problem. This implicitly assumes that such fluctuations represent realizations of multidimensional Gaussian probability densities. As mentioned,  $C_D$  incorporates the errors in the surface seismic data and in the forward modeling procedure and  $C_M$  incorporates the a priori uncertainties related to layered subsurface models.

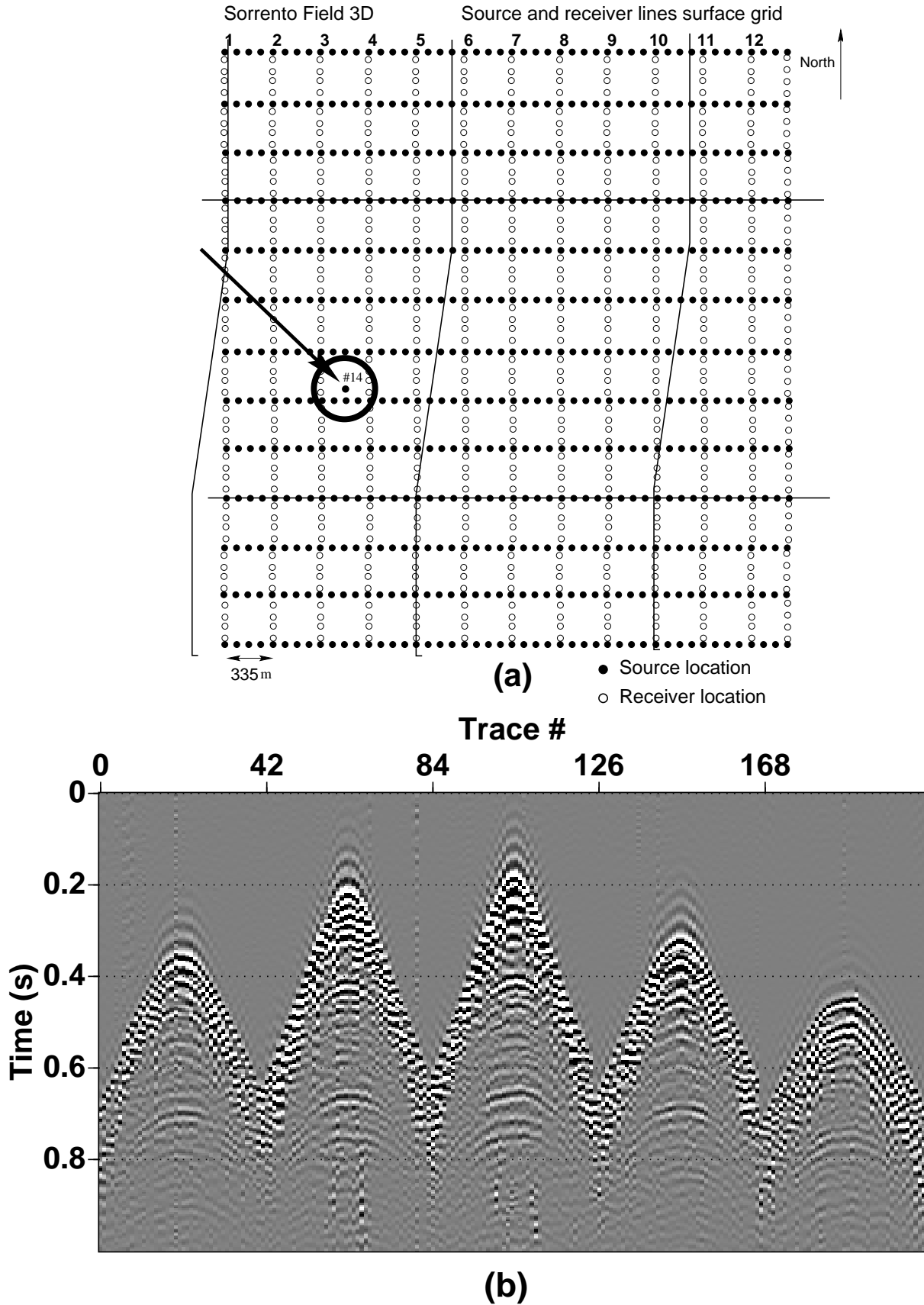


**Figure 2.** (a) Intended source and receiver positions for the 3-D Sorrento survey. The shot gathers within the circle will be denoted shots 1 to 5, starting from the leftmost one. The arrow indicates the location of the well MULL 14. (b) Lines 1, 2, 4, 5 and 6 of shot gather 1. Receiver-group spacing is 67 m, receiver-line spacing is 335 m and time sampling interval is 4 ms.

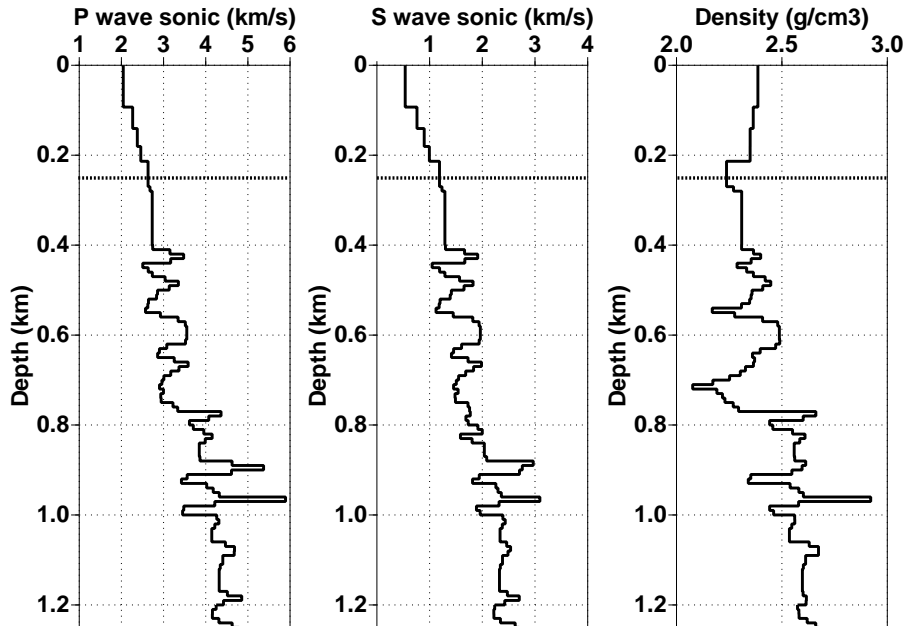


**Figure 3.** Well logs acquired at Mull 14 after median filtering and blocking. The target depth interval for the inversion is 1 km thick and goes from 0.25 km (dashed line) to 1.25 km. The discretization interval is 10 m.

#### 4.1. Model Uncertainties

Here, we construct the a priori probability density  $\rho(\mathbf{m})$  from P wave and S wave sonic and density logs. The motivation for doing so is to incorporate information about the subsurface that is consistent with well logs, whether such information is constrained by the seismic data or not. This avoids ad hoc preconceptions about the degree of model smoothness. Indeed, model smoothness can be used to stabilize the maximum-likelihood optimization procedure (Tikhonov regularization), but it is not strictly necessary in the Bayesian approach. (In principle, it is not necessary to invert any operators to construct the solution, which is the a posteriori probability, or inferences derived from this function. Thus it is correct, although slightly unconventional, to say that there is no such thing as an ill-posed Bayesian inverse problem.) Here we estimate the correlation among model parameters from the well log measurements and see to what extent this is influenced a posteriori by the seismic data. We represent  $\rho(\mathbf{m})$  by a multidimensional Gaussian probability density (second expression in equation (2)), whose parameters (the mean  $\mathbf{m}_{\text{prior}}$  and the covariance matrix  $C_M$ ) are obtained from the sonic and density logs. The prior  $\mathbf{m}_{\text{prior}}$  (Figure 4) is computed by applying a 200-m running average to the log data. The prior model  $\mathbf{m}_{\text{prior}}$  is

also used to incorporate the kinematics of the seismic data reflection events, which are defined by this long-wavelength trend of the subsurface parameters. The procedure to estimate the model covariance matrix  $C_M$  is shown in Figure 5 for the P wave impedance log. (The P wave impedance and S wave impedance logs were obtained by the product of the P wave velocity and density in the first case and S wave velocity and density in the second. Throughout, the units used for impedances and density are  $10^5 \text{ g s}^{-1} \text{ cm}^{-2}$  and  $\text{g cm}^{-3}$ , respectively.) This amounts to computing the autocorrelation of the fluctuations of the well log about  $\mathbf{m}_{\text{prior}}$  within a sliding window, which accounts for the fact that both mean and variance of the well log change with depth. The double arrow in Figure 5 shows the length of the autocorrelation window. Once the correlation  $\mathcal{C}(\tau)$  is computed for a given window, the model covariance matrix is given by

$$\begin{aligned} C[i, j] &= \mathcal{C}(j - i) \\ &= \frac{1}{N + 1} \sum_{k=i-\frac{N}{2}}^{i+\frac{N}{2}} L(k) L(k + j - i). \end{aligned} \quad (5)$$

$N$  is the length of the sliding window centered at depth  $i \, dz$ ,  $L(k)$  is the well log sample at depth  $k \, dz$ , and  $dz$  is the depth discretization interval. Three covariance matrices result from this procedure: one for the P

wave impedance, one for the S wave impedance and one for density (Figure 6). These matrices are used to form a block diagonal covariance matrix  $C_M$ . At this point, no cross correlation between different parameters is being considered. The amplitudes along the main diagonal of this matrix correlate with the variance of the fluctuations of the well log about  $\mathbf{m}_{\text{prior}}$ . For instance, the large fluctuations at depths around 950 m can be seen in the covariance matrix by the large variances at indices around  $i, j = 70$ . Notice that the indices of the covariance matrix are the same as the ones of the model vector  $\mathbf{m}$  used to parameterize the subsurface. Those are defined as  $(z_1 - z_0)/dz$ , where  $z_1$  is the depth of a given layer,  $z_0$  is the initial depth of the target zone, and  $dz$  is the depth discretization level used in the inverse calculation. Here  $z_0 = 250$  m and  $dz = 10$  m. Thus the index value of 70 for  $z_1 = 950$  m.

The a priori model covariance matrices define our prejudices about the subsurface, without taking into account the surface seismic data. For instance, Figure 7 shows the a priori standard deviations given by the square roots of the main diagonal elements of the three model covariances in Figure 6. These standard deviations define an interval about  $\mathbf{m}_{\text{prior}}$  within which the true subsurface parameters are assumed to lie with a certain degree of confidence. Learning about a particular parameter from the surface seismic data means reducing and/or relocating these intervals. If the data do not provide any information about a parameter, the a priori knowledge about this parameter will remain unchanged. This is easily understood by looking at the expression of the a posteriori covariance matrix when a Gaussian approximation is used for the a posteriori probability density  $\sigma(\mathbf{m})$ ,

$$C_{M'} = [G^T C_D^{-1} G + C_M^{-1}]^{-1}. \quad (6)$$

If the data are not informative, the term  $G^T C_D^{-1} G$  will go to zero and  $C_{M'} = C_M$ . As the data become more informative, this term will increase, thus reducing the uncertainties about the subsurface parameters.

## 4.2. Data Uncertainties

The data covariance matrix  $C_D$  in the likelihood  $L(\mathbf{m})$  function defines the uncertainties in the data, both observational and theoretical (modeling) uncertainties. It is possible to show [Tarantola, 1987] that assuming all uncertainties are Gaussian,  $C_D$  consists of the sum of the covariances associated with each type of uncertainty. This result will be used here to incor-

porate into the calculation both types of data uncertainties. Specifically, we considered (1) ambient noise, (2) near-surface heterogeneities (residual statics), (3) scaling factor between field and synthetic data, and (4) model discretization errors. Therefore the final data covariance matrix  $C_D$  is given by

$$\begin{aligned} C_D &= C_{OBS} + C_{MOD} \\ C_{OBS} &= C_D^{AN} + C_D^{ST} \\ C_{MOD} &= C_D^{SC} + C_D^{DS}, \end{aligned} \quad (7)$$

where the superscripts AN, ST, SC and DS refer to ambient noise, residual statics, scaling factor and discretization, respectively. The addition of the covariance matrices  $C_D^{AN}$  and  $C_D^{ST}$  to form  $C_{OBS}$  and of the covariance matrices  $C_D^{SC}$  and  $C_D^{DS}$  to form  $C_{MOD}$  is justified because the uncertainties due to the ambient noise and near surface, as well as the uncertainties due to the scaling factor and model discretization, can be considered independent.

The elements along the main diagonal of these matrices are the variances of the fluctuations about the mean of the Gaussian probability densities that characterize the uncertainties, and the off-diagonal elements show to what extent these fluctuations are correlated. For practical calculations the means of these densities are defined by the observed data  $\mathbf{d}_{\text{obs}}$  for the observational uncertainties and the synthetic data  $g(\mathbf{m} = \text{well log})$  for the modeling uncertainties, generated for the well log measurements shown in Figure 3. Strictly speaking, the covariance matrix associated with modeling errors should be independent of the model  $\mathbf{m}$ . Therefore the underlying hypothesis in the approach presented here is that the matrix  $C_{MOD}$  can be estimated for a single model (defined by the well log measurements) and used throughout in the inversion process. An alternative procedure is to estimate this covariance matrix for an ensemble of models and to select the one associated with the largest uncertainties, thus using a worst-case covariance matrix in the inversion.

The calculation of the covariance matrices is similar for all items listed above in the sense that in all cases it boils down to the estimation of a covariance matrix from an ensemble of  $N$  “noise” seismograms  $\mathbf{s}_i$ . The noise seismograms should represent fluctuations about the mean of the underlying probability density that models the uncertainty under consideration. Once realizations of such probabilities are constructed, the noise seismograms are obtained by subtracting the appropriate mean,  $\mathbf{d}_{\text{obs}}$  in the case of observational uncertainties and  $g(\mathbf{m} = \text{well log})$  in the case of

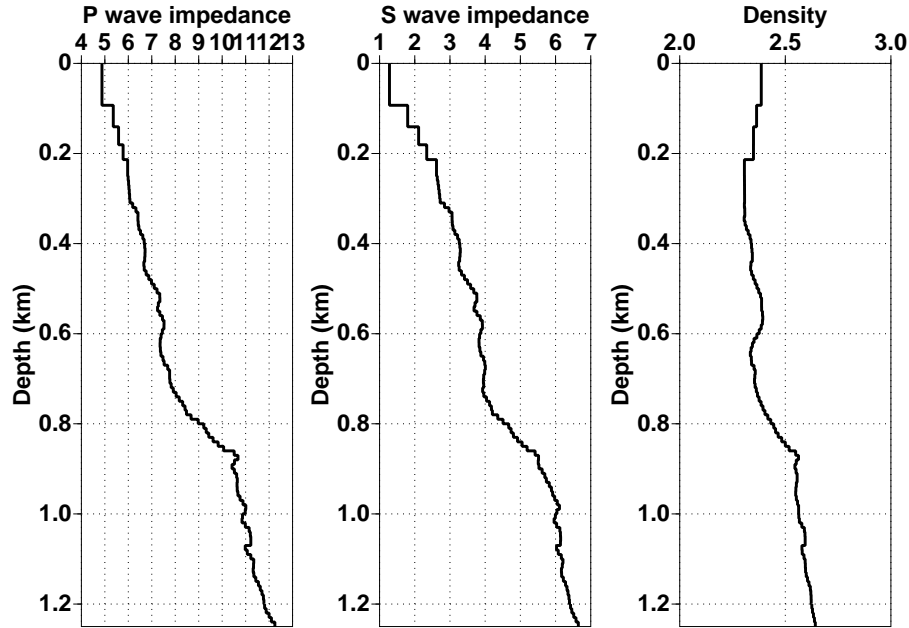


**Figure 4.** The a priori model  $\mathbf{m}_{\text{prior}}$  used in the inversion of the Sorrento data. This model was obtained by a running average of the well log data shown in Figure 3.

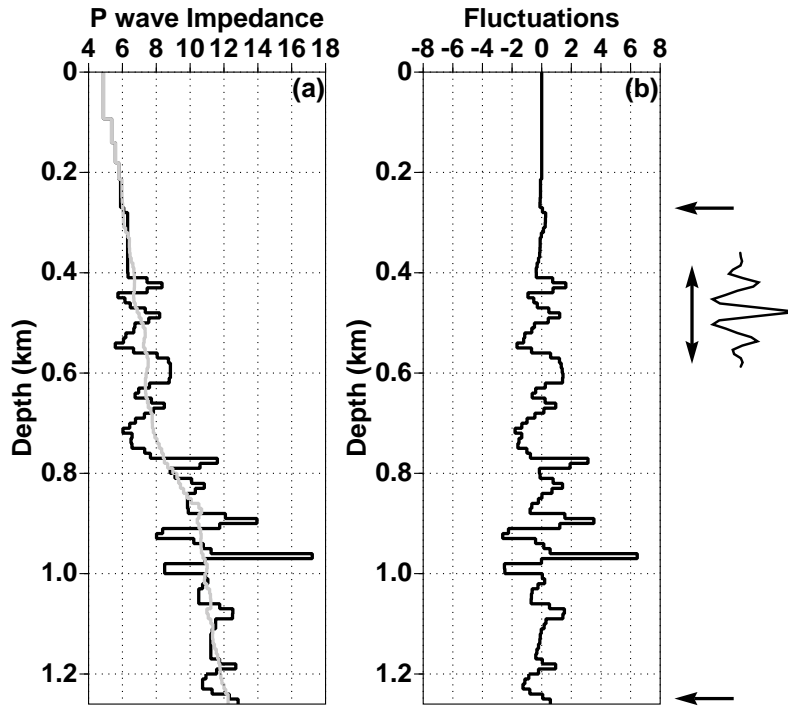


**Figure 5.** Illustration of the technique to compute the a priori covariance matrix from well log measurements. (a) P wave impedance log (bold line) and  $\mathbf{m}_{\text{prior}}$  (gray line), derived from that profile with a running average procedure. (b) The fluctuations of the well log about  $\mathbf{m}_{\text{prior}}$ , which will be used in the computation of the model covariance matrix. The vertical double arrow shows the length of the autocorrelation window. The two horizontal arrows indicate the target depth zone, within which the covariance matrix is computed.

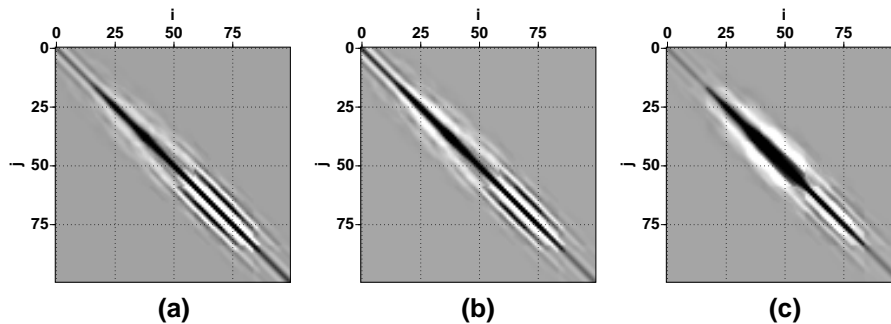


**Figure 6.** We have parameterized the subsurface with 100 horizontal layers of 10 m thickness with 3 parameters for each layer (P wave and S wave impedance and density). The covariance matrices (100 by 100)  $C[i, j]$  are shown for the fluctuations of the measured values (well log MULL 14) of these parameters about the running mean of the log. (a) P wave impedance, (b) S -wave impedance, and (c) density.

modeling uncertainties, from these realizations. Then one estimator of the covariance matrix from  $N$  of those seismograms is given by *Priestley* [1981]

$$\hat{C} = \frac{1}{N} \sum_{i=1}^N \mathbf{s}_i \mathbf{s}_i^T. \quad (8)$$

Note that the dimension of the (square) data covariance matrix  $C_D$  should be the same as the data misfit vector  $g(\mathbf{m}) - \mathbf{d}_{\text{obs}}$  in the likelihood function. Therefore the noise seismograms  $\mathbf{s}_i$  should be of the same length as the data misfit window, 1 s in this calculation, resulting in a covariance matrix of dimensions 251x251 (the time-sampling interval is 4 ms). Next we briefly describe the procedure used to construct the noise seismograms for all types of uncertainties considered. A full description is given by *Gouveia* [1996].

#### 4.3. Ambient Noise

Here the noise seismograms  $\mathbf{s}_i$  represent samples of the ambient noise in the data. These are constructed from time windows prior to the first arrivals, within which it is assumed no significant source-generated signal has been recorded. For this purpose, we used the samples of the first 0.1 s of the Sorrento data to form several 1-second long noise seismograms  $\mathbf{s}_i$  by simply concatenating the samples from adjacent seismograms. Those seismograms are assumed to be realizations of the probability density that characterizes the ambient noise. Thus expression (8) can be used to estimate an ambient noise covariance matrix. The noise seismograms are shown in Figure 8. The covariance matrix is shown in Figure 9a. Essentially, this matrix has a single main diagonal band, the width of

which shows the degree of ambient noise correlation, about 20 samples (0.08 s) in this case.

#### 4.4. Near-Surface Heterogeneities

In the inversion of the Sorrento data the near surface model, which includes depths down to 250 m, was derived from well logs and kept fixed throughout the inversion process. This model, consisting of the five layers above the horizontal dashed lines shown in Figure 3, obviously represents an oversimplification of the complexity associated with the true near surface. Accounting for all uncertainties associated with the near surface is a difficult, if not impossible, task. Some of these uncertainties, however, can be taken into account. Specifically, we considered errors in the residual statics estimation procedure. This was done by corrupting the data with random surface consistent statics and then computing the data difference between the original and corrupted data sets. The artificial residual statics introduced in the data were uniformly distributed between  $[-8 \text{ ms}, 8 \text{ ms}]$ , which represents a 40% error in the estimated residual statics of the data. These data residuals quantify the fluctuations about the observed data due to uncertainties in the residual static values, and were used to estimate the covariance matrix shown in Figure 9b.

#### 4.5. Scaling Factor Between Seismic and Synthetic Data

An inversion procedure based on data fitting generally requires a scaling, or calibration, factor between synthetic and field data. Here, this was done by minimizing the least squares misfit between the nearest-offset field seismic traces acquired at line 3 of shot 1 with synthetic seismograms computed for the well log

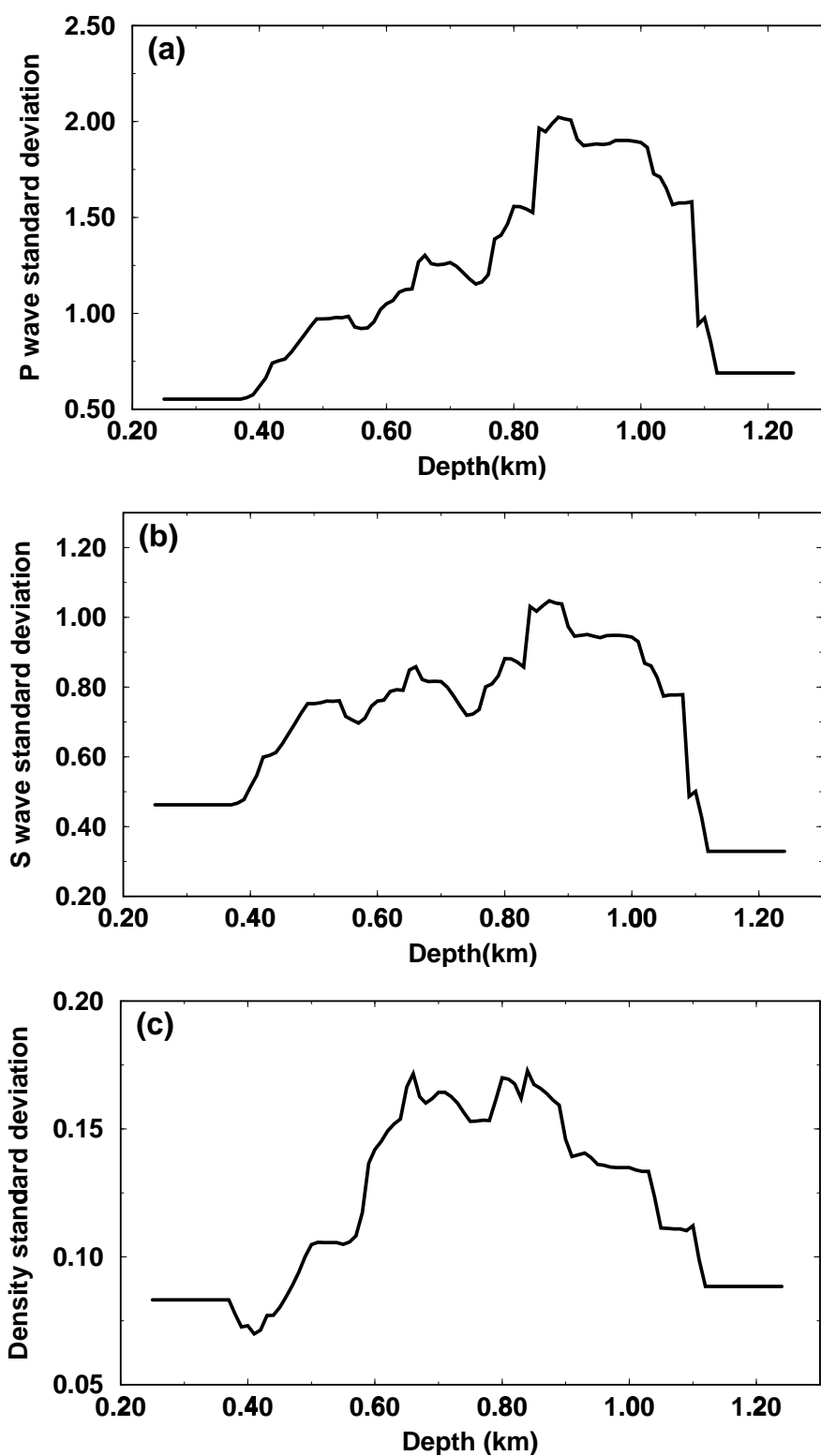


**Figure 7.** A priori standard deviations (square roots of the main diagonal elements of the a priori model covariance matrices (Figure 6)). (a) P wave impedance, (b) S wave impedance, and (c) density.

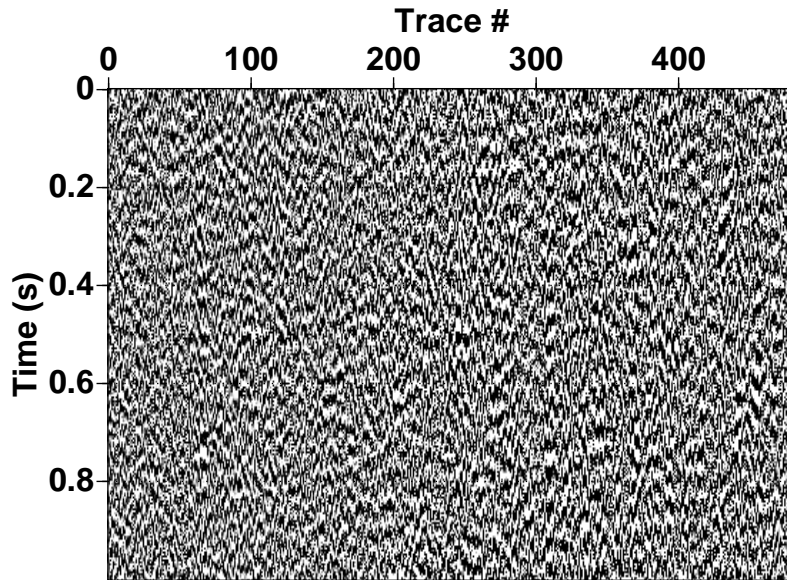


**Figure 8.** Noise seismograms constructed from realizations of ambient noise in the seismic traces. Those realizations are assumed to be characterized by a multidimensional Gaussian process and were obtained by windowing the first 0.1 s of the Sorrento data. Within this time window no significant source-generated energy can be noticed.

MULL 14 (Figure 3) for a given time window. We used a reflectivity modeling algorithm with a point force excitation to generate the synthetic seismograms. The source signature consists of a zero-phase wavelet, band limited from 2 to 60 Hz, and computed from the inverse Fourier transform of a Hanning window. We consider this source signature accurate enough for the purpose of reproducing the field data, as will be shown in section 5.

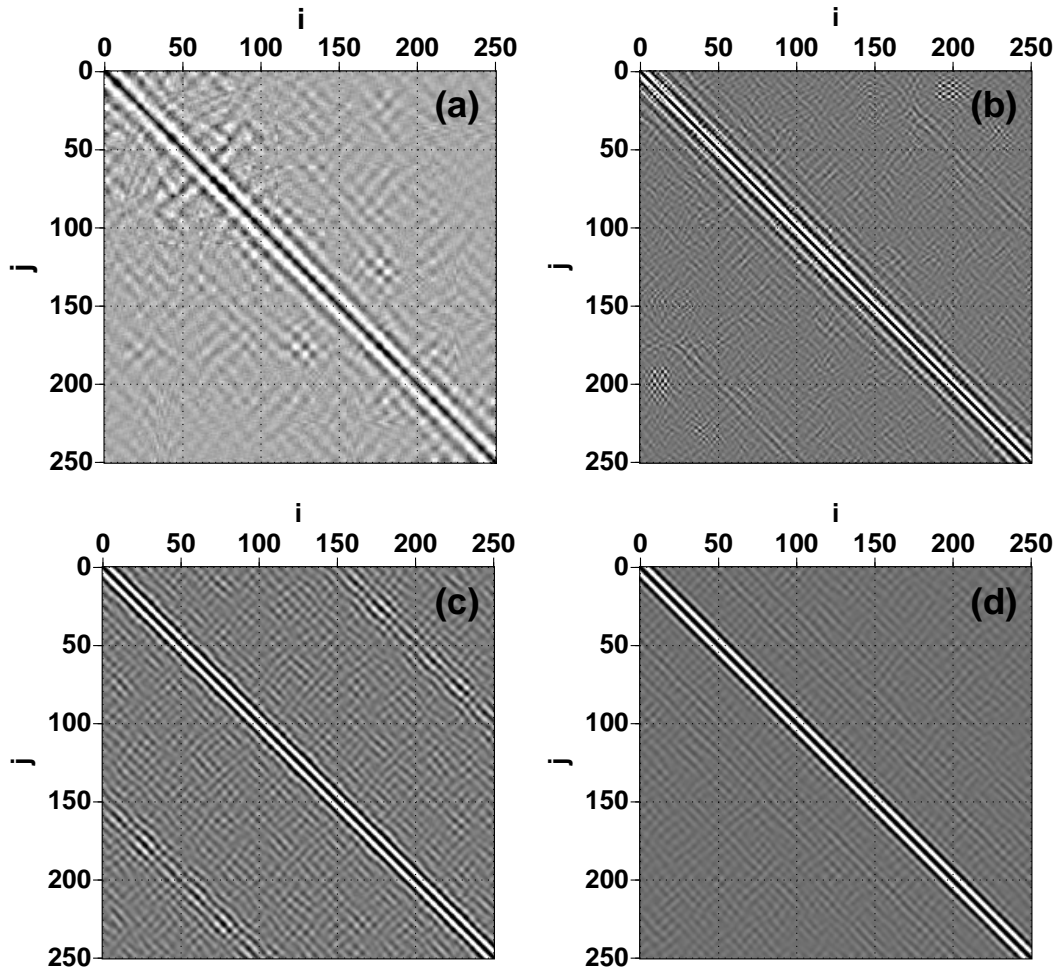
This procedure is subject to uncertainties related to the well log measurements and also to the choice of the wavelet used in the synthetics. These issues motivate the incorporation of the uncertainties related to this scaling factor into the calculation. As with the other covariance matrices, this is done by computing a covariance matrix from the fluctuations about the mean of the Gaussian probability density that models the uncertainty associated with the scaling factor. This mean is taken to be the synthetic data generated for the well log scaled by the optimum factor. The fluctuations are the differences between this data set and the synthetic data generated for the well log but now scaled by different factors that represent errors up to 20% in the optimum scaling factor. Specifically, such factors were defined to be 0.80, 0.85, 0.90, and 0.95 times the optimum one. We have then used those data fluctuations to estimate the covariance matrix associated with the scaling factor uncertainties shown in

Figure 9c.

#### 4.6. Model Discretization Errors

An important a priori assumption made in the inversion of the Sorrento data set is that the subsurface can be described by a laterally homogeneous medium. Once this is done it remains to be determined how many layers should be used in the parameterization of the subsurface model. We opted for a model parameterization consisting of 100 layers, each with constant thickness of 10 m. This choice was driven by computational considerations.

The purpose of a model covariance matrix associated with discretization errors is to incorporate into the calculation errors due to the parameterization of a continuous or piecewise-continuous medium by a discrete 100-layer model. As mentioned, we assume that a Gaussian multidimensional probability density is suitable to characterize these errors. The mean of this probability is the synthetic seismic data generated for the blocked well log (Figure 3). Fluctuations about this mean can be computed from its difference with the synthetic seismic data set generated for the full nonblocked well log. These fluctuations are used to estimate a discretization error covariance matrix, which is shown in Figure 9d.



**Figure 9.** Covariance matrices associated with (a) ambient noise, (b) near-surface, (c) scaling-factor, and (d) discretization errors. In each case the covariance matrix was computed from realizations of the underlying process, assumed to be multidimensional Gaussian.

#### 4.7. Discussion

As mentioned in section 4.2, the final data covariance matrix is the sum of the covariance matrices associated with each one of the sources of uncertainties (Figure 9). The elements of the main diagonal of the resulting matrix are the variances of the total data errors, and the width of the main diagonal indicates to what extent the data uncertainties are correlated. This matrix should be regarded as an average covariance matrix, since it was built from the entire data set used in the inversion. Although possible, we have not attempted to estimate an individual data covariance matrix for each of the gathers of the survey.

In this calculation the largest uncertainties are associated with the discretization errors, while the smallest are those associated with the amplitude scaling factor. It is, however, important to emphasize that the following assumptions have been made to quantify such uncertainties:

1. The noise seismograms represent realizations of the underlying probability densities that model the specific noise under consideration. These probability densities are assumed to be multidimensional Gaussian functions.

2. There is negligible source-generated signal in the 0.1 s window of the seismic data taken to represent the ambient noise, and correlations in this noise are no larger than the length of this window.

3. The distortions imposed by the near surface on the reflection seismic data can be modeled by surface consistent residual statics. Errors in residual statics estimation are therefore related to the uncertainty of subsurface estimates due to near-surface heterogeneities. Here, we assumed that such errors are uniformly distributed within  $[-8 \text{ ms}, 8 \text{ ms}]$ , which implies a maximum error of 40% in the residual statics applied to the Sorrento data.

4. The magnitude of the error in the scale factor is limited to 20% of its optimum value.

5. The full nonblocked well log measurements can be used to quantify the uncertainties associated with the model discretization.

It is not clear to us how best to carry out a sensitivity analysis of the resulting covariance matrices to these assumptions without having to repeat the whole calculation for different choices in the construction of the covariance matrices. Although we believe such an analysis is important, it is beyond the scope of this paper.

Obviously, not all possible uncertainties have been accounted for. For example, uncertainties related to anisotropy, absorption, lateral velocity variations, and three-dimensional structures have been ignored. For the specific case of Sorrento we have accepted the information that three-dimensional structural features, geological dip, lateral velocity variations at shot point scale, and anisotropy are not an issue. Therefore we have not considered these sources of errors. In general, however, such errors must be accounted for if the corresponding physical effects contribute significantly to the data.

#### 5. Explaining the Recorded Data

The maximum a posteriori (MAP) model is derived from an iterative optimization process that maximizes  $\sigma(\mathbf{m})$ , defined as the product of the two functions in equation (2). This is equivalent to the minimization of the following objective function:

$$\Theta(\mathbf{m}) = \frac{1}{2} [(g(\mathbf{m}) - \mathbf{d}_{\text{obs}})^T C_D^{-1} (g(\mathbf{m}) - \mathbf{d}_{\text{obs}}) + (\mathbf{m} - \mathbf{m}_{\text{prior}})^T C_M^{-1} (\mathbf{m} - \mathbf{m}_{\text{prior}})]. \quad (9)$$

We have used a nonlinear conjugate gradient algorithm equipped with a line search procedure [Dennis and Schnabel, 1987] in the minimization. (See Deng et al. [1996] for information on how to obtain this and other optimization codes from the CWP Object-Oriented Optimization Library.) The a priori model  $\mathbf{m}_{\text{prior}}$ , shown in Figure 4, was chosen as the initial model for the optimization. This model is perturbed by the optimization procedure until it fits the observed data to approximately one noise standard deviation, considering both data errors and forward modeling errors. Thus, the stopping criterion is

$$(g(\mathbf{m}) - \mathbf{d}_{\text{obs}})^T C_D^{-1} (g(\mathbf{m}) - \mathbf{d}_{\text{obs}}) \leq N, \quad (10)$$

where  $C_D$  is given by equation (7) and  $N$  is the number of observations. The wavelet used in the calibration of field and synthetic data was used throughout in the inversion process. All 25 gathers were inverted for P wave impedance, S wave impedance, and density profiles, yielding 25 MAP subsurface models. The initial guess was the same for all gathers and so were the data and model covariance matrices.

Figure 10 shows the MAP models and associated a posteriori error bars derived from the shot gathers shown in Figure 2. The error bars shown in Figure 10 are the square roots of the main diagonal elements of the a posteriori covariance matrix (6), to be discussed

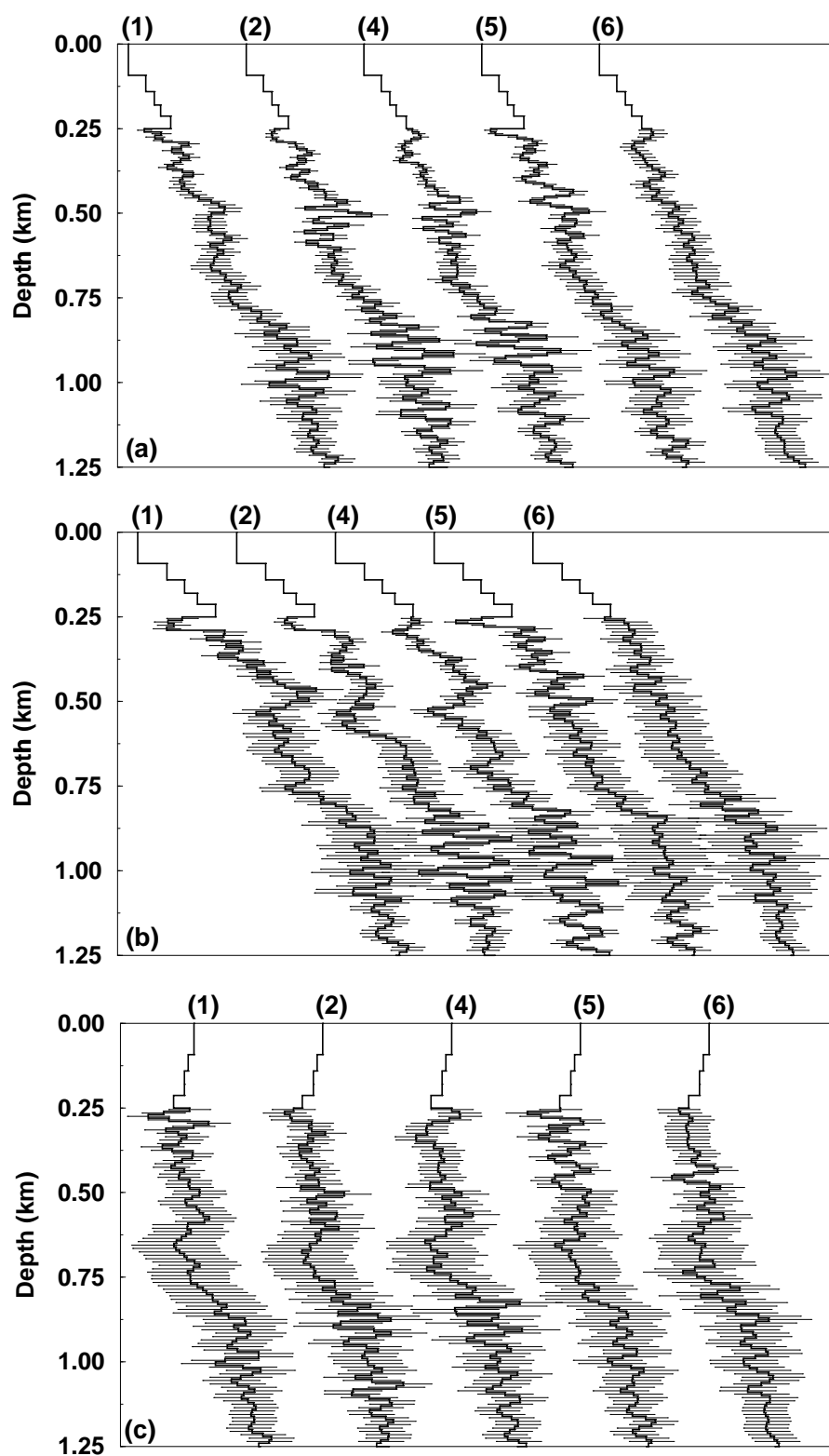


**Figure 10.** MAP models derived from shot gather 1 (Figure 2): (a) P wave impedance profiles. (b) S wave impedance profiles, and (c) density profiles. The numbers at the top of each profile are associated with the line numbers. The error bars are  $\pm$  unit standard deviations derived from the a posteriori covariance matrix.

in section 6. The number of nonlinear conjugate gradient iterations needed to compute the MAP models ranged from 3 (for lower quality gathers) to 8 (for gathers with better signal content).

The synthetic data computed for each of the MAP models are shown in Figure 11, along with the data residuals. Comparison with the observed data illustrated in Figure 2 demonstrates that MAP models explain the data to a large extent. We believe the residuals are mainly associated with slightly nonhyperbolic reflections due to mild lateral velocity variations present in the Sorrento field. Such nonhyperbolic events cannot be modeled with an elastic isotropic reflectivity modeling algorithm, since the reflectivity method does not take into account lateral inhomogeneities of the subsurface. Moreover, this lateral correlation in the residuals is not accounted for by the Gaussian probability densities used here to model a priori uncertainties and therefore illustrates one limitation of the proposed approach.

## 6. Uncertainty Analysis

All questions related to uncertainties associated with the MAP models presented in section 5 have to be addressed via the a posteriori probability density  $\sigma(\mathbf{m})$ . The complicated nature of this function (due to the nonlinearity associated with the reflectivity integral) would seem to require Monte Carlo sampling procedures for this uncertainty analysis. Considering the dimensionality of the problem and the high computational cost of the modeling algorithm, Monte Carlo sampling methods are not feasible without vastly greater computational resources than were available to us. As a compromise, the resolution analysis of the parameter estimates will be based on the Gaussian approximation of the a posteriori probability  $\sigma_g(\mathbf{m})$  (equation (3)).

For the Sorrento data there are 25 a posteriori covariance matrices  $C_{M'}$ , each one associated with a given MAP model. A typical matrix (the one computed for line 4 of shot gather 1) is shown in Figure 12. This  $3 \times 3$  block matrix shows the autocorrelation of the P wave impedance, S wave impedance, and density on its main block diagonal and the cross-correlation among different parameters in the off-diagonal blocks. The structure of this matrix is similar to the covariance matrices associated with the other MAP models. The energy in the off-diagonal blocks indicates the degree of coupling among different parameters. Since the a priori model covariance is block

diagonal (no cross correlations among the three subsurface parameter types were considered in this problem) and the data covariance matrix is quasi-diagonal, the nonzero elements in the off-diagonal blocks of  $C_{M'}$  are due to the Jacobian  $G$  in equation (6). In other words, the cross-correlation elements in the a posteriori covariance are due to correlations of the synthetic wave field generated when, for instance, a P wave impedance and a density of a given layer are disturbed. The extent to which such wave fields are distinct is related to the degree of data resolution for those two specific parameters.

Although the structure of the data covariances is similar for different MAP models, the magnitude of the elements is not. This is shown in Figure 13, which compares the a posteriori standard deviations (square roots of the main diagonal of  $C_{M'}$ ) with the a priori standard deviations (square roots of the main diagonal of  $C_M$ ). Figure 13 provides insight into the different degree of data resolution for P wave impedance, S wave impedance, and density by showing to what extent the a priori error bars are reduced when including the data in the inversion procedure. The P wave impedance is the best resolved parameter, followed by the S wave impedance and then density. This is not surprising since the surface data consist of vertical component seismograms. Notice that for density, virtually no reduction in the standard deviation was observed. The only result of the inversion for this parameter was to recenter the a priori probability density from  $\mathbf{m}_{\text{prior}}$  to  $\mathbf{m}_{\text{map}}$ .

Inspection of Figure 13 shows a correlation between the reduction of the a priori standard deviations and the data quality (or signal-to-noise ratio) of the gathers displayed in Figure 2. This is easier to show if we consider two specific shot gathers, situated at extremes in data quality. Those gathers, shown in Figure 14, were extracted from line 4 of shot 1 and line 7 of shot 5 (Figure 2), respectively. It is clear from these data that one gather is much more informative about the subsurface than the other, due to its higher signal content. This statement is quantitatively confirmed by Figure 15 which shows the a priori standard deviations and a posteriori standard deviations derived from both gathers. The reduction of the a priori standard deviations is greater for the data with better signal-to-noise ratio.

The standard deviations (or error bars) provide a limited view of the uncertainties associated with the inverse problem. By focusing just on the a priori and a posteriori error bars (Figures 13 and 15) one is neg-

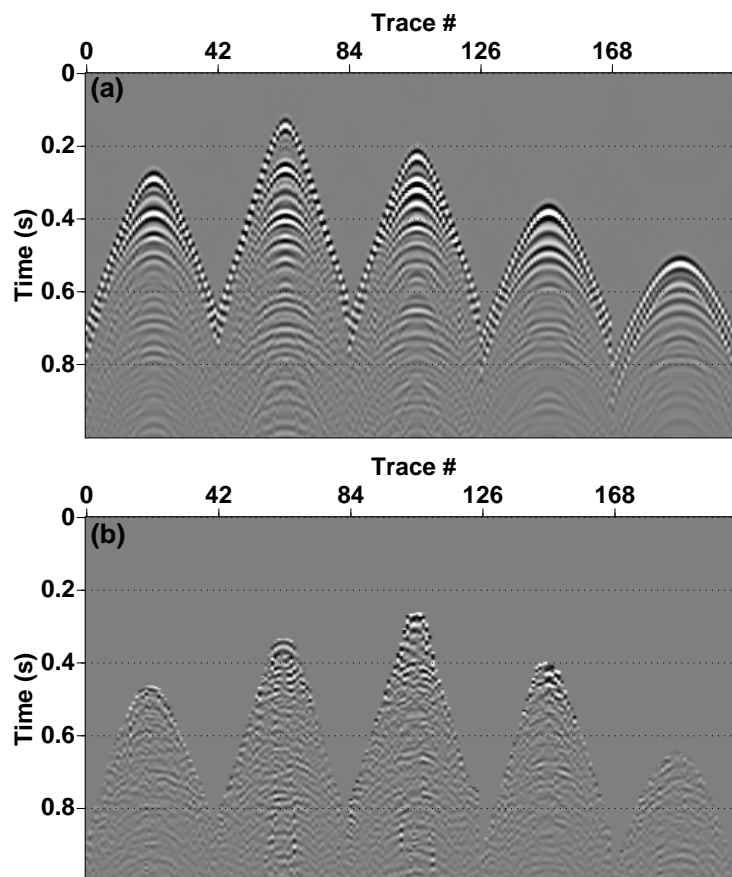


**Figure 11.** (a) Synthetic data and (b) data residuals associated with the MAP models illustrated in Figure 10. Note that the residuals have been muted for the first arrivals. These events were not considered in the data misfit window since they are related to the near-surface layers which are outside the target zone defined for the inverse problem.

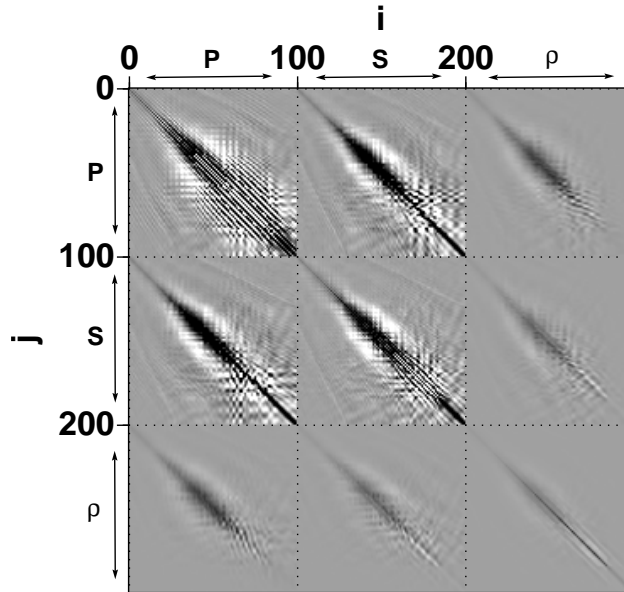


**Figure 12.** A *posteriori* covariance matrix for the MAP model estimated from line 4 of shot gather 1 (Figure 2). The labels **P**, **S** and  $\rho$  indicate P, S wave impedance and density, respectively.

lecting the off-diagonal elements of the respective covariance matrices. Sampling the underlying probability densities,  $\rho(\mathbf{m})$  and  $\sigma_g(\mathbf{m})$ , to generate pseudo-random realizations of the subsurface incorporates all the information available in  $C_M$  and  $C_{M'}$ , respectively. Moreover, examining these pseudo-random models side by side can be useful in unveiling subtle subsurface features that are resolved by the data. Laterally coherent features that are present in most of the realizations of the a posteriori probability density  $\sigma_g(\mathbf{m})$  and are not present in the realizations of the a priori probability density  $\rho(\mathbf{m})$  are associated with high confidence subsurface estimates obtained from the surface seismic data.

Here, the sampling procedure is done by taking the inner product of the lower triangular part of the  $LU$  decomposition of the covariance matrix, with an uncorrelated Gaussian pseudo-random sequence of zero mean and unit variance [Parker, 1994]. Figure 16 shows the realizations obtained by sampling the a priori probability density  $\rho(\mathbf{m})$ . The only apparent feature that those models have in common is the long-wavelength trend given by  $\mathbf{m}_{\text{prior}}$ .

Figures 17 and 18 show the pseudo-random subsurface realizations obtained by sampling the a posteriori probability density  $\sigma_g(\mathbf{m})$  associated with the seismic gathers shown in Figure 14. As expected, P wave realizations tend to show the smallest degree of

variation, followed by the S wave realizations and then density. For shot 1 it is possible to identify a number of laterally coherent features in the P wave impedance realizations. A smaller number of these features can be observed in the S wave impedance and density realizations. In spite of the fact that the inversion did not reduce the error bars for density, some structure is seen in the pseudo-random realizations of this parameter. This structure is due to the MAP density models (Figure 10c) that show features not present in the model  $\mathbf{m}_{\text{prior}}$ . All realizations associated with the gather extracted from shot 5 show little continuity and are similar to the a priori pseudo-random realizations (Figure 16).

Visual comparison of the a priori realizations (Figure 16) with the a posteriori ones (Figure 17 and Figure 18) provides insight into the surface seismic data resolution on the subsurface parameters. Such resolution is higher at depths where short-wavelength features, which are absent in the a priori realizations, are laterally continuous in Figures 17 and 18.

Finally, a third mechanism to assess the uncertainties associated with the inverse calculation is the use of marginal probability densities. With the Gaussian probabilities  $\rho(\mathbf{m})$  and  $\sigma_g(\mathbf{m})$ , these marginals can be computed analytically [Miller, 1964]. Figures 19, 20 and 21 show the a priori and a posteriori marginals for the P wave impedance, S wave impedance

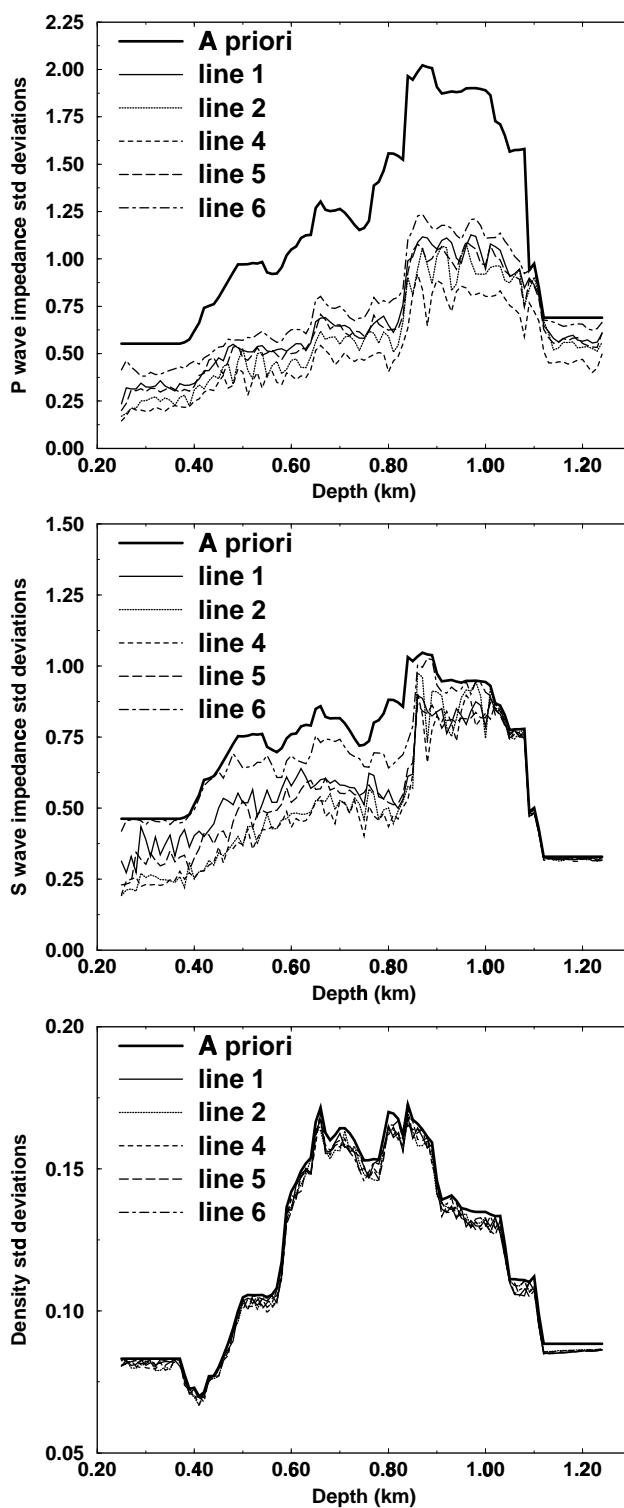
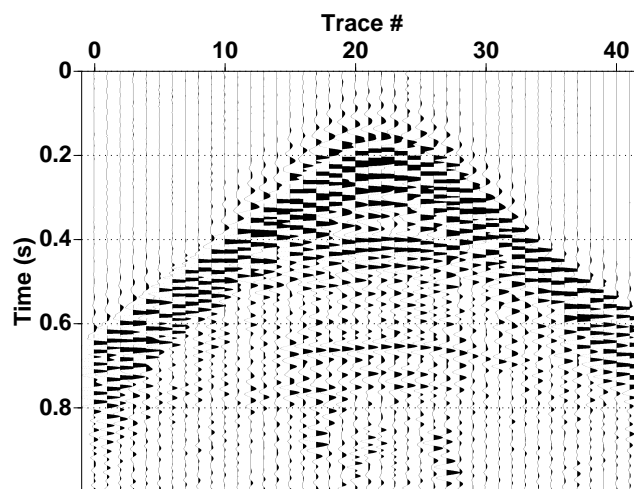
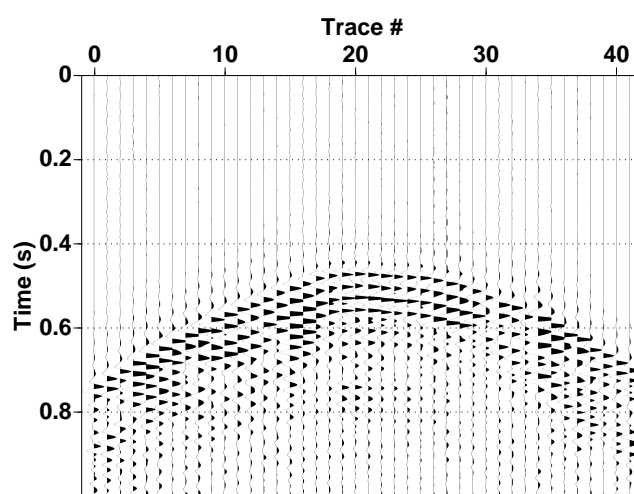


**Figure 13.** Comparison of a priori and a posteriori standard deviations for the MAP models estimated from shot gather 1.



(a)



(b)

**Figure 14.** Shot gathers extracted (a) from line 4 of shot 1 and (b) from line 7 of shot 5 (b) of the Sorrento data. There is essentially no signal in the gather extracted from shot 5, other than the refracted arrivals from the near surface, which were not used as data for the inversion.

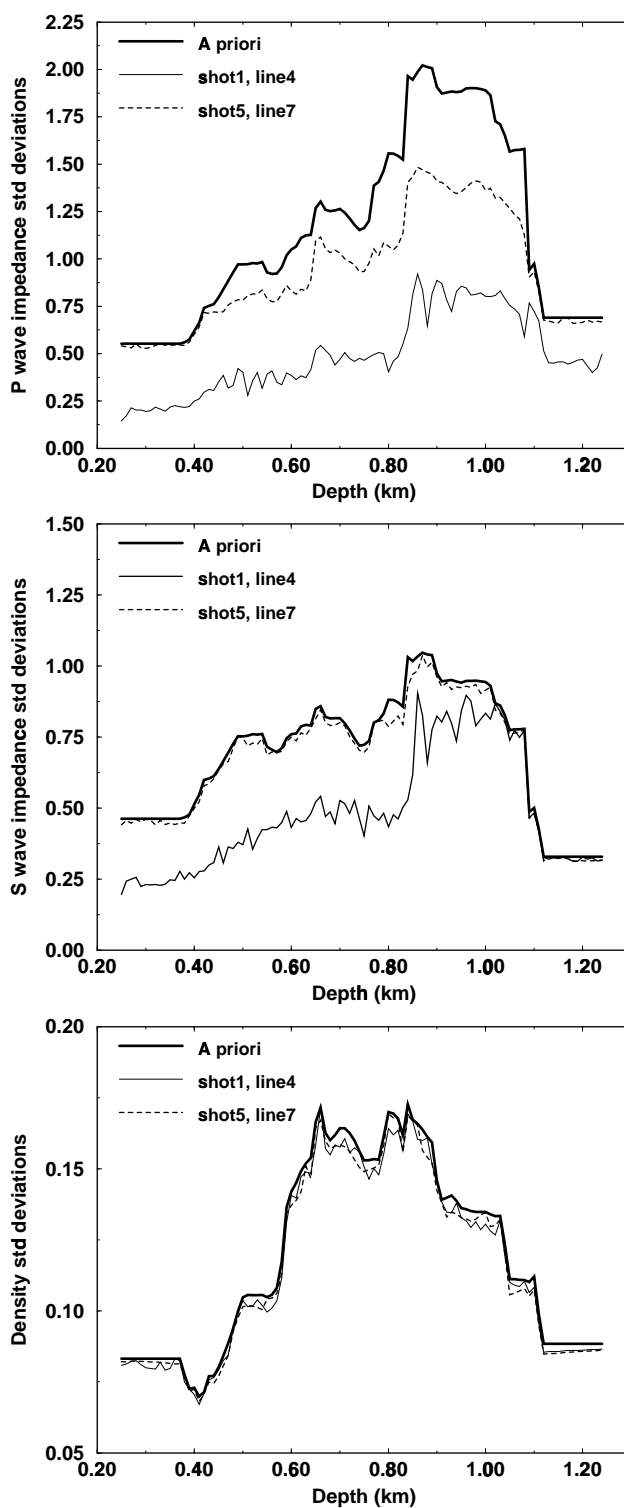


**Figure 15.** A posteriori standard deviations relative to the gathers shown in Figure 14, representing cases of best and worst of data quality.

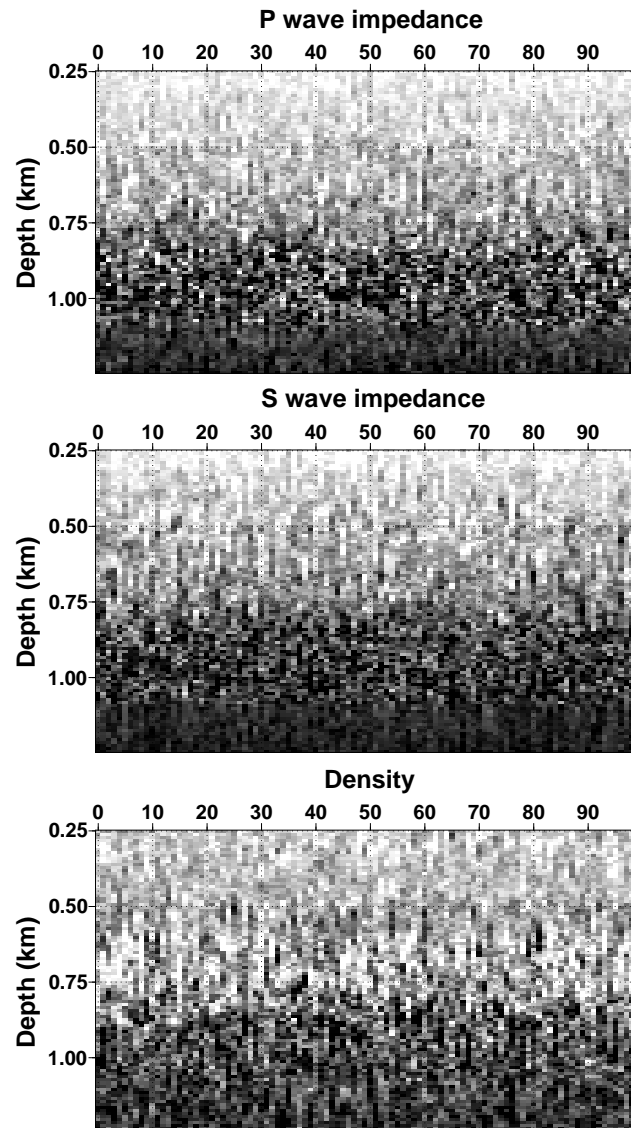


**Figure 16.** One hundred pseudo-random realizations samples from the a priori probability density  $\rho(\mathbf{m})$ . Note that this is not a single subsurface laterally varying model; it is 100 different laterally invariant depth models shown side by side.

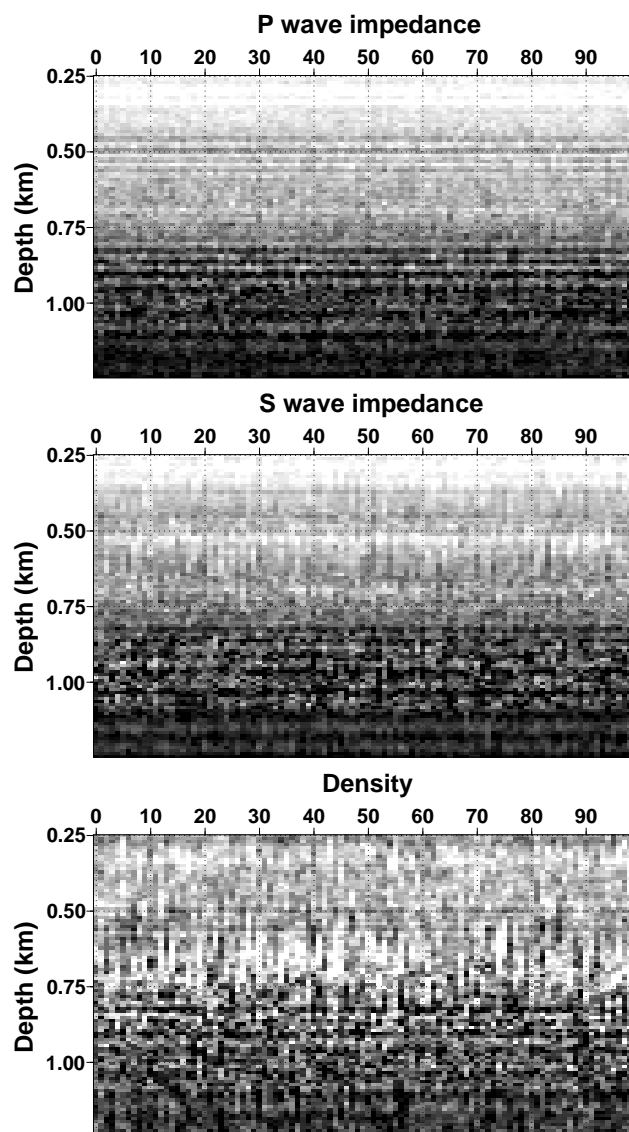


**Figure 17.** One hundred a posteriori pseudo-random realizations of the subsurface generated for the gather extracted from shot 1 (illustrated in Figure 14a). Best resolved parameter is P wave impedance, followed by S wave impedance and density.

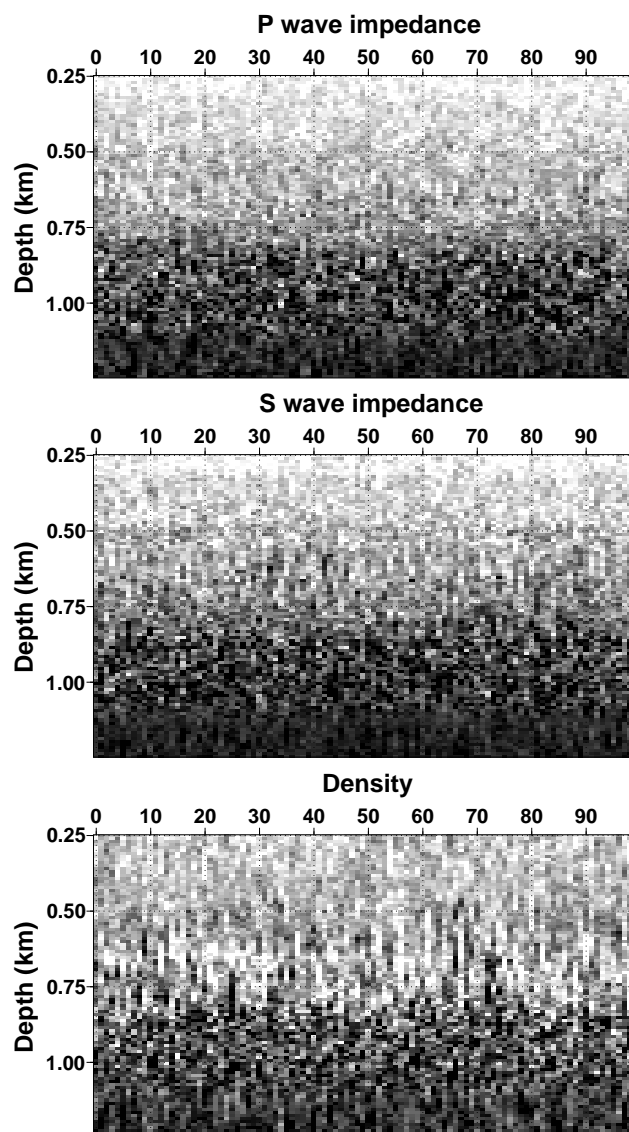


**Figure 18.** One hundred a posteriori pseudo-random realizations of the subsurface generated for the gather extracted from shot 5 (illustrated in Figure 14b). Little or no resolution is provided by the data for any of the subsurface parameters.

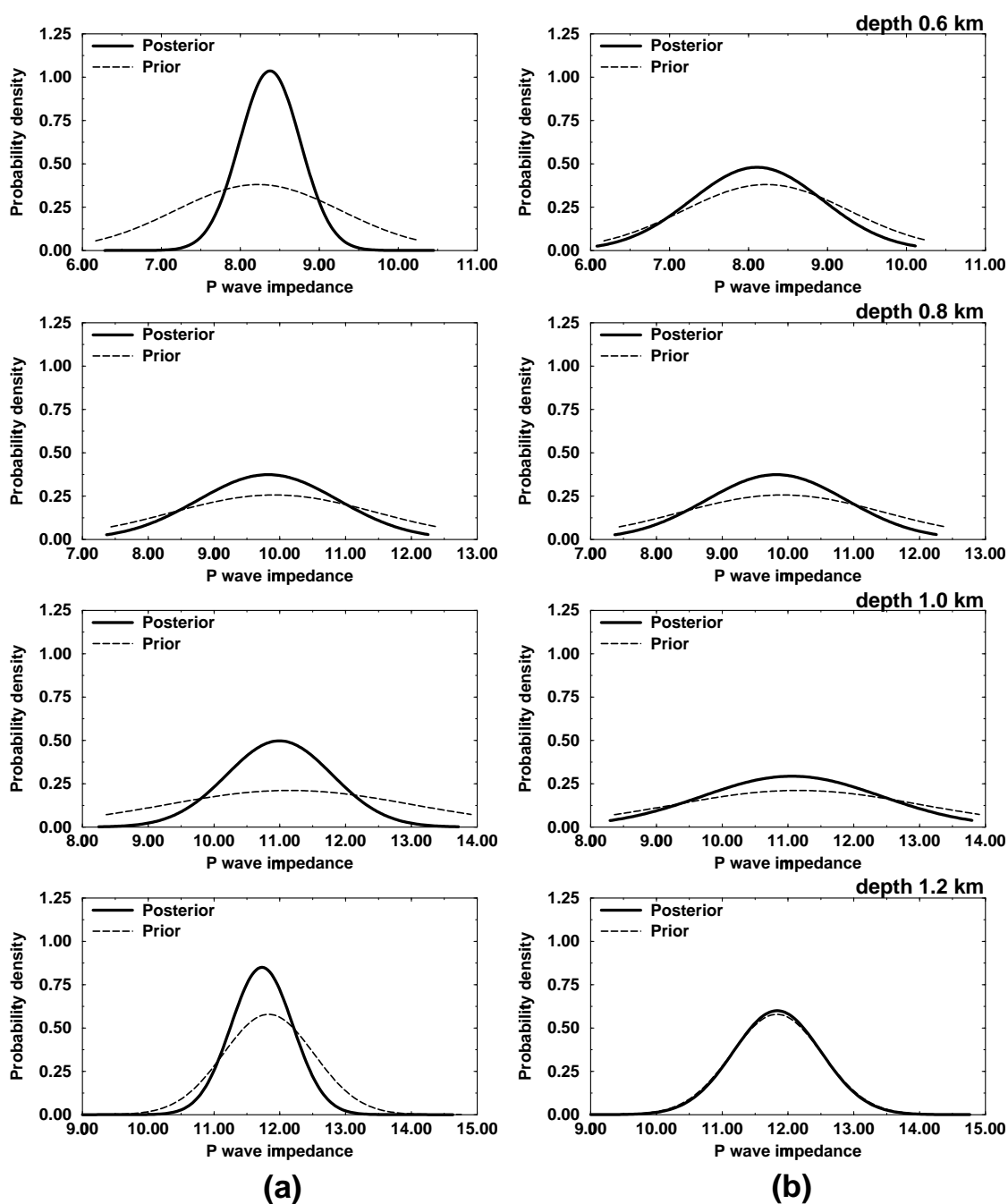


**Figure 19.** P wave impedance marginals, at depths 0.6 km, 0.8 km, 1.0 km and 1.2 km. (a) Marginals associated with the data extracted from line 4 of shot gather 1 (Figure 14a). (b) shows the marginals associated with the data extracted from line 7 of shot gather 5 (Figure 14b).

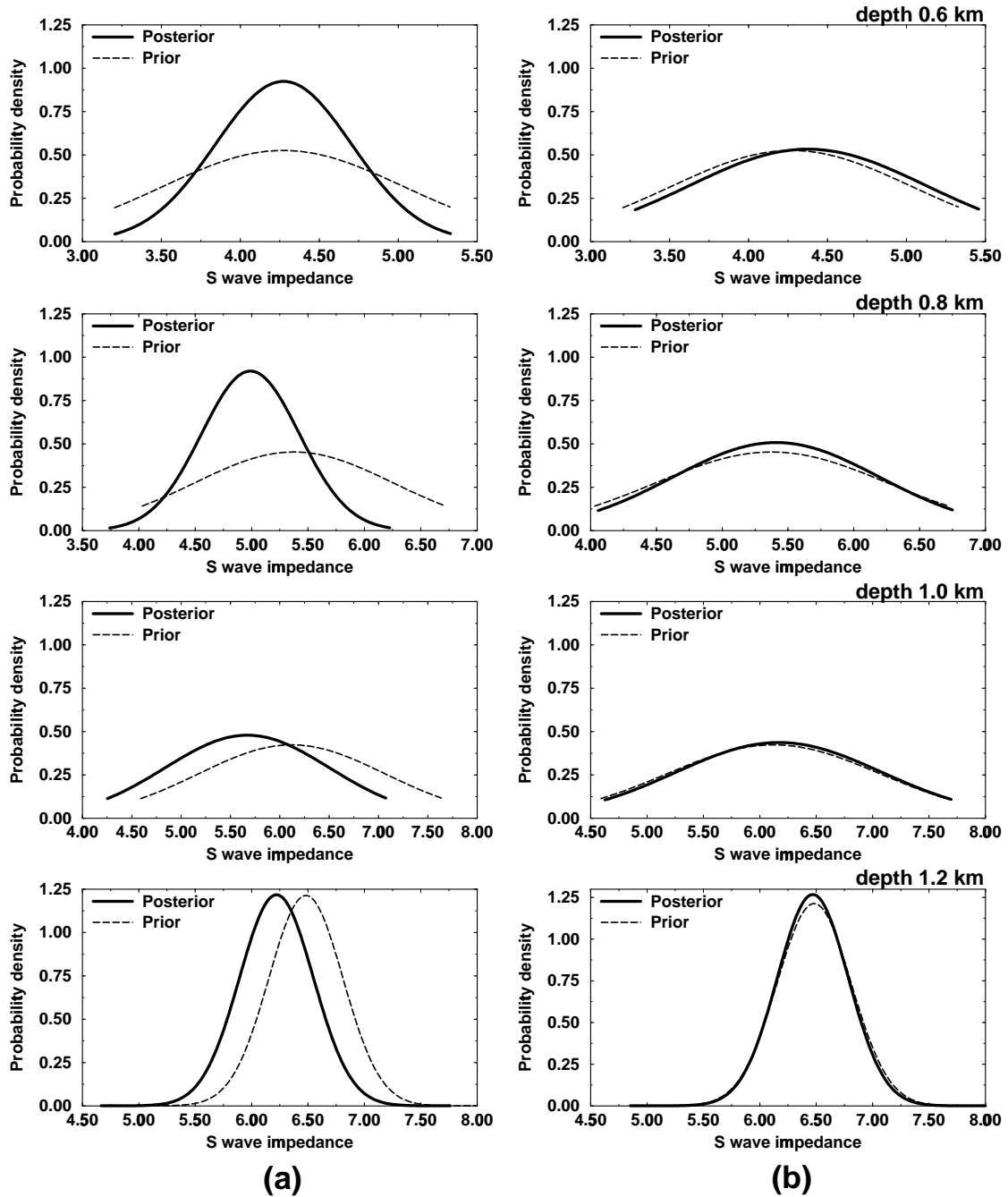


**Figure 20.** S wave impedance marginals, at depths 0.6 km, 0.8 km, 1.0 km and 1.2 km. (a) Marginals associated with the data extracted from line 4 of shot gather 1 (Figure 14a) (b) Marginals associated with the data extracted from line 7 of shot gather 5 (Figure 14b).

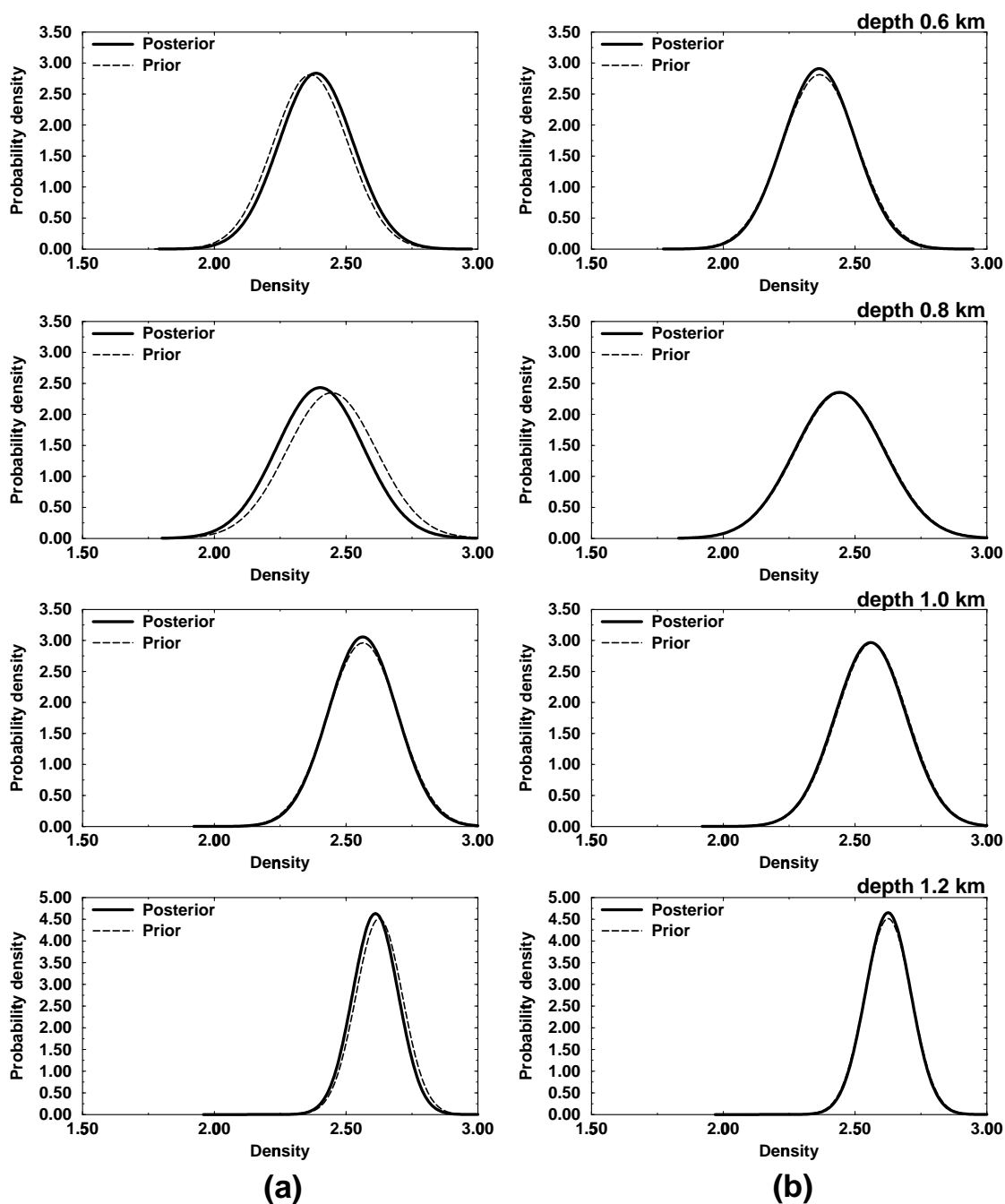


**Figure 21.** Density marginals, at depths 0.6 km, 0.8 km, 1.0 km and 1.2 km. (a) Marginals associated with the data extracted from line 4 of shot gather 1 (Figure 14a). (b) Marginals associated with the data extracted from line 7 of shot gather 5 (Figure 14b).

and density at four distinct depths: 0.6 km, 0.8 km, 1.0 km and 1.2 km. These functions were obtained for the same gathers displayed in Figure 14. Consistent with the standard deviations shown in Figure 15 and the pseudo-random realizations shown in Figures 17 and 18 the data from line 4 of shot gather 1 have a much larger degree of resolution than the data from line 5 of shot gather 7.

Using these marginals, we can answer specific questions about the parameters. For instance, the probability that the P wave impedance at a depth of 0.6 km is between 8 and 9  $10^5 \text{ g s}^{-1} \text{ cm}^{-2}$  is about 0.82. If we denote the marginal probability of the P wave impedance  $m_P$  by  $p(m_P)$ , then the probability  $\mathbf{P}$  that  $m_P$  is within the range  $[m_P^1, m_P^2]$  is given by

$$\mathbf{P} = \int_{m_P^1}^{m_P^2} p(m_P) dm_P. \quad (11)$$

Questions involving more than one parameter can also be addressed. For example, what is the probability  $\mathbf{P}$  that the P wave impedance and density of a given layer are limited by a certain interval, such as  $[m_P^1, m_P^2]$  and  $[m_\rho^1, m_\rho^2]$ , respectively? This probability is derived from the marginal probability density  $p(m_P, m_\rho)$  associated with those two parameters, and it is given by

$$\mathbf{P} = \int_{m_P^1}^{m_P^2} \int_{m_\rho^1}^{m_\rho^2} p(m_P, m_\rho) dm_P dm_\rho. \quad (12)$$

Obviously, more elaborate questions involving more parameters of the subsurface have to be addressed by integrating the multidimensional marginals associated with these parameters. Equations (11) and (12) are simple examples of how the a posteriori probability  $\sigma(\mathbf{m})$  can be used to answer questions that might be posed by the seismic interpreter. Although one of the objectives of this work is to propose a methodology by which this probability can be built honoring the uncertainties in the data, forward modeling operator, and subsurface parameters, we also want to emphasize the numerous difficulties encountered and the many assumptions required along the way of assessing uncertainties in a realistic seismic inversion calculation.

## 7. Conclusions

There have many examples of the use of Bayesian inference in geophysics. What has been noticeably missing, however, at least in seismic data inversion, are field data case studies which make a fair and

realistic attempt to estimate the required probability densities from data and other information. Our goal was to show such an example, steering a middle ground between the most general Bayesian approach, which might require Monte Carlo sampling of a nonlinear a posteriori probability density, and an optimization-based approach (e.g., least squares) that does not seriously address the uncertainties in the data or model parameters. Within a fully Gaussian framework, we have shown such a case study in which statistical inferences are made from reflection seismic data which take into account ambient noise, near surface effects, uncertainty in amplitude scaling, and model discretization errors. Further, we have computed a multidimensional Gaussian a priori probability density for layered models from in situ petrophysical measurements. These sources of information are assimilated via Bayes theorem into probabilistic statements about the subsurface. We presented distillations of this a posteriori probability information in three ways: as the maximum a posteriori model bracketed by one standard deviation error bars, as typical models pseudo-randomly sampled from this probability density function, and as marginal probabilities for the individual parameters. We also contrasted the Bayesian MAP model, which must not only fit the surface seismic data but the well log data as well, with the smoothest model that fits the seismic data alone (the Occam model). From this we saw that the Bayesian MAP model has many features not implied by the surface data, and hence without the well log, there would be an enormous range of models consistent with the surface data alone. Therefore the a priori information was important in narrowing the range of models consistent with the seismic data. Finally, it is clear that all uncertainty analysis carried out in this work relies upon the adequacy of a Gaussian model for the multidimensional probability densities required by the Bayesian approach. To get beyond (or simply test) this approximation for the problem under consideration may require a significantly different strategy since we believe that Monte Carlo sampling of arbitrary probabilities would be infeasible for multioffset reflection seismic data.

All codes used in this work were written in ANSI C and parallelized over a network of workstations and shared-memory multiprocessors using the Parallel Virtual Machine (PVM) message-passing library. The codes include the reflectivity-based forward modeling and Fréchet derivative calculations, the nonlinear conjugate gradient optimization, and all the tools needed

to estimate and analyze the covariance matrices. They are freely available from the WEB site

[http://www.cwp.mines.edu/inverse\\_theory](http://www.cwp.mines.edu/inverse_theory).

**Acknowledgments.** This work was partially supported by the sponsors of the Consortium Project on Seismic Inverse Methods for Complex Structures at the Center for Wave Phenomena, Colorado School of Mines, the Army Research Office under grant DAAH04-95-1-0173, and the National Science Foundation under grant DMS-9506603.

## References

- Constable, S.C., and R.L. Parker, Occam's inversion: A practical algorithm for generating smooth models from electromagnetic sounding data, *Geophysics*, *52*, 289–300, 1987.
- Cruse, E., A. Pica, M. Noble, J. McDonald, and A. Tarantola, Robust elastic nonlinear waveform inversion: Application to real data, *Geophysics*, *55*, 527–538, 1990.
- Deng, H.L., W. Gouveia, and J.A. Scales, The CWP Object-Oriented Optimization Library, *The Leading Edge*, *15*, 365–369, 1996.
- Dennis, J., and R. Schnabel, *Numerical Methods for Unconstrained Optimization*. Prentice-Hall, Englewood Cliffs, N.J., 1987.
- Fuchs, K., and G. Mueller, Computation of synthetic seismograms with the reflectivity method and comparison with observations, *Geophys. J.*, *11*, 417–433, 1971.
- Gouveia, W., and J.A. Scales, Resolution of seismic waveform inversion: Bayes vs. Occam, *Inverse Problems*, *13*, 323–349, 1997.
- Gouveia, W. P., Bayesian seismic waveform data inversion: Parameter estimation and uncertainty analysis, Ph.D. thesis, Colo. Sch. of Mines, Golden, 1996.
- Mark, S., Characterizing compartmentalization of a petroleum reservoir by integrating sequence stratigraphy, 3-D seismic interpretation, and production data, Sorrento field, Colorado, USA, Ph.D. thesis, Colo. Sch. of Mines, Golden, 1995.
- Miller, K., *Multidimensional Gaussian Distributions*. Wiley, New York, 1964.
- Mora, P., Nonlinear two-dimensional elastic inversion of multi-offset seismic data. *Geophysics*, *52*, 1211–1228, 1987.
- Mosegaard, K., and A. Tarantola, Monte Carlo sampling of solutions to inverse problems, *J. Geophys. Res.*, *100*, 12431–12447, 1995.
- Parker, R.L., *Geophysical Inverse Theory*, Princeton Univ. Press, Princeton, N.J., 1994.
- Priestley, M. B., *Spectral Analysis of Time Series Analysis*, Academic Press, San Diego, Calif., 1981.
- Scales, J.A., Uncertainties in Seismic Inverse Calculations, pp. 79–97 in *Inverse Methods*, edited by B.H. Jacobson, K. Mosegaard, and P. Sibani, Springer-Verlag, New York, 1996.
- Scales, J.A., and R. Snieder, To Bayes or not to Bayes, *Geophysics*, *62*, 1045–1046, 1997.
- Stark, P.B., Minimax confidence intervals in geomagnetism, *Geophys. Jour. International*, *108*, 329–338, 1992.
- Tarantola, A., *Inverse Problem Theory*. Elsevier, New York, 1987.

---

W.P. Gouveia and J.A. Scales, Department of Geophysics, Colorado School of Mines, Golden, CO 80401. (e-mail: wpgouvei@dal.mobil.com; jscales@mines.edu)

January 23, 1997; revised July 29, 1997; accepted October 9, 1997.

---

<sup>1</sup>Now at Mobil E & P Technical Center, Dallas, TX.